The Astrophysical Journal, 755:103 (10pp), 2012 August 20 doi:10.1088/0004-637X/755/2/103

GLANCING VIEWS OF THE EARTH: FROM A LUNAR ECLIPSE TO AN EXOPLANETARY TRANSIT

A. García Muñoz[1,2], M. R. Zapatero Osorio[3], R. Barrena[1,2], P. Montañés-Rodríguez[1,2], E. L. Martín[3], and E. Pallé[1,2]
[1] Instituto de Astrofísica de Canarias, C/Vía Láctea s/n, E-38205 La Laguna, Tenerife, Spain; tonhingm@gmail.com
[2] Departamento de Astrofísica, Facultad de Física, Universidad de La Laguna, E-38071 La Laguna, Tenerife, Spain
[3] Centro de Astrobiología, CSIC-INTA, Ctra. de Torrejón a Ajalvir, km 4, E-28550 Madrid, Spain
Received 2012 March 8; accepted 2012 June 12; published 2012 August 1

ABSTRACT

It has been posited that lunar eclipse observations may help predict the in-transit signature of Earth-like extrasolar planets. However, a comparative analysis of the two phenomena addressing in detail the transport of stellar light through the planet's atmosphere has not yet been presented. Here, we proceed with the investigation of both phenomena by making use of a common formulation. Our starting point is a set of previously unpublished near-infrared spectra collected at various phases during the 2008 August lunar eclipse. We then take the formulation to the limit of an infinitely distant observer in order to investigate the in-transit signature of the Earth–Sun system as being observed from outside our solar system. The refraction bending of sunlight rays that pass through Earth's atmosphere is a critical factor in the illumination of the eclipsed Moon. Likewise, refraction will have an impact on the in-transit transmission spectrum for specific planet–star systems depending on the refractive properties of the planet's atmosphere, the stellar size, and the planet's orbital distance. For the Earth–Sun system, at mid-transit, refraction prevents the remote observer's access to the lower ∼12–14 km of the atmosphere and, thus, also to the bulk of the spectroscopically active atmospheric gases. We demonstrate that the effective optical radius of the Earth in-transit is modulated by refraction and varies by ∼12 km from mid-transit to internal contact. The refractive nature of atmospheres, a property which is rarely accounted for in published investigations, will pose additional challenges to the characterization of Earth-like extrasolar planets. Refraction may have a lesser impact for Earth-like extrasolar planets within the habitable zone of some M-type stars.

Key words: Earth – planets and satellites: atmospheres – techniques: spectroscopic

Online-only material: color figures

1. INTRODUCTION

The contemplation of the Moon during a lunar eclipse reveals the dimming, and subsequent brightening, of the lunar disk as the satellite enters, and then exits, the shadow cast by the Sun-illuminated Earth. For decades, ground-based observers have constructed light curves of the sunlight reflected from the eclipsed Moon (e.g., Link 1962; García Muñoz & Pallé 2011 and references therein). The experiment is relevant to the investigation of the terrestrial atmosphere because, for a known position of the Moon within Earth's shadow, the light curves are interpretable in terms of the optical properties of the atmosphere (Ugolnikov & Maslov 2006, 2008). Beyond traditional photometric measurements, two spectroscopic observations of the 2008 August lunar eclipse have demonstrated the richness of the spectrum of sunlight reflected from the eclipsed Moon and shown that it contains the signature of the principal atmospheric constituents (Pallé et al. 2009; Vidal-Madjar et al. 2010).

Within the sample of known extrasolar planets, the transiting ones form a subgroup particularly apt for characterization. During transit, the planet partially blocks the disk of its host star, causing a drop in the amount of stellar light that arrives to the observer. The apparent stellar dimming is related to the sizes of the core and—when there is one—the gaseous envelope of the planet. The technique of in-transit transmission spectroscopy, which relies on comparing the apparent stellar dimming at selected wavelengths, has led to the detection of atoms and molecules such as Na, H, C, O, CO, CO_2, H_2O, and CH_4 in the atmospheres of a few giant close-in extrasolar planets (e.g., Charbonneau et al. 2002; Vidal-Madjar et al. 2003, 2004; Tinetti et al. 2007; Désert et al. 2009; Sing et al. 2009; Swain et al. 2009). The same technique, applied to GJ 1214b, is helping elucidate whether this so-called super-Earth (Charbonneau et al. 2009) might contain abundant water in its atmosphere (Berta et al. 2012).

Lunar eclipses and exoplanetary transits are related phenomena. In both instances, a fraction of the light collected by the observer is stellar light that has passed through a section of the planet's limb and, thus, carries the signature of the planet's gaseous envelope. The photon trajectories, whether direct or deflected in scattering collisions with the atmospheric constituents, determine the signature imprinted on the collected stellar light. Throughout the text, we use the term (lunar) eclipse to refer to the alignment of the Sun, Earth, and Moon, and transit to refer to Earth's passage in front of the Sun as observed from a remote vantage point.

The classical theory of lunar eclipses assumes that refracted sunlight, rather than the scattered component, determines the brightness of the eclipsed Moon (Link 1962). However, García Muñoz et al. (2011) have shown that both components may become comparably intense under conditions of elevated aerosol loading. With a few exceptions or brief references (Seager & Sasselov 2000; Brown 2001; Hubbard et al. 2001; Hui & Seager 2002; Ehrenreich et al. 2006; Kaltenegger & Traub 2009; Sidis & Sari 2010), the effect of refraction on the light curves of transiting extrasolar planets has largely been ignored. The omission is likely due to the minor contribution of refraction to the light curves of the close-in giant planets that constitute most of the extrasolar planets discovered to date. However, and as shown below, refraction has a non-negligible impact for smaller planets far out from their host stars.

As the newly discovered extrasolar planets steadily approach terrestrial sizes (e.g., Charbonneau et al. 2009; Léger et al. 2009; Mayor et al. 2009; Batalha et al. 2011; Lissauer et al. 2011), further attention is being devoted to the prediction of the in-transit signature of Earth-like extrasolar planets. In preparation for future observations, a number of recent works have investigated the potential of in-transit transmission spectroscopy for the characterization of such targets (e.g., Ehrenreich et al. 2006; Kaltenegger & Traub 2009; Pallé et al. 2011; Rauer et al. 2011). In that context, it has been suggested that lunar eclipse spectra may help test the strategies that will eventually lead to the characterization of Earth-like extrasolar planets (Pallé et al. 2009; Vidal-Madjar et al. 2010).

Our paper investigates the transport of stellar light through Earth's atmosphere in lunar eclipses and exoplanetary transits. Our main goal is to clarify the similarities and dissimilarities in the signal collected by terrestrial observers in both types of event, emphasizing the impact of refraction. The paper is structured in two main parts. In the first part, Sections 2 and 3, we introduce the lunar eclipse theory and investigate a set of previously unpublished near-infrared spectra of the 2008 August lunar eclipse. In the second part, Section 4, we take the lunar eclipse theory to the limit of a remotely distant observer and address the comparison between lunar eclipses and transits. In Sections 3 and 4, we also discuss the conclusions drawn by some prior works in relation with the theory of lunar eclipses and exoplanetary transits. Finally, Section 5 summarizes the main conclusions. To the best of our knowledge, this is the first work that investigates the effect of refraction on the in-transit spectral signature of Earth-like extrasolar planets.

2. THE DATA. THE LUNAR ECLIPSE THEORY

The spectra investigated in Section 3 were obtained on 2008 August 16 with the LIRIS spectrograph at the William Herschel Telescope (WHT; Manchado et al. 1998), located at the Observatorio del Roque de los Muchachos (ORM), La Palma, Spain. The observations were made alternating over two wavelength ranges with two different grisms: zj, from 0.9 to 1.5 μm, and hk, from 1.4 to 2.4 μm. A total of 11 spectra of the Moon in umbra were collected, 6 in zj and 5 in hk. The umbra observations ran from 20:54 until 22:16 UT and probed different phases of Earth's inner shadow projected on the lunar disk. The data reduction and telluric correction follow Pallé et al. (2009) and will not be discussed further. The FITS raw datafiles are publicly available from the ING Archive.[4] For their published spectrum from 1 to 2.4 μm, Pallé et al. (2009) merged the three spectra closest to greatest eclipse in each wavelength range. We will now focus on the individual umbra spectra in order to investigate their evolution over time and distance from greatest eclipse.

For the interpretation of the observations, we produced model simulations of the eclipse spectrum. The simulations involved solving the radiative transport problem of sunlight in Earth's atmosphere according to the formulation laid out by García Muñoz & Pallé (2011). The formulation assumes that the observer is located on the Moon's surface, which allows us to ignore the reflection of sunlight at the Moon and the atmospheric extinction above the Earth-bound observer.

Generally, we integrate the direct and scattered components of radiance at the lunar observer's site over a solid angle $\partial\Omega$ that includes both the solar and planetary disks. Denoting by

[4] http://casu.ast.cam.ac.uk/casuadc/archives/ingarch

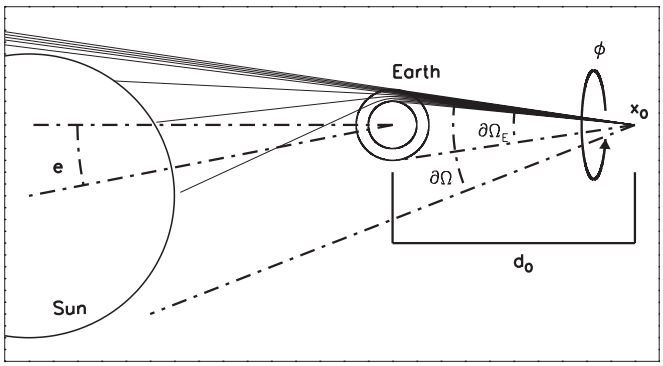

Figure 1. Sketch of the Earth–Sun system and the ray tracing scheme from the observer's site toward the Sun. Each ray is characterized by an incident direction $\mathbf{s}_O$ at the observer's site $\mathbf{x}_O$. The elementary surface for evaluating the irradiance at $\mathbf{x}_O$ is oriented with its normal vector $\mathbf{n}_{\mathbf{x}_O}$ following the line that joins $\mathbf{x}_O$ and the planet's center.

$L(\mathbf{x}_O, \mathbf{s}_O)$ the radiance at the observer's site $\mathbf{x}_O$ in the incident direction $\mathbf{s}_O$, the irradiance or flux of sunlight into an elementary surface oriented according to $\mathbf{n}_{\mathbf{x}_O}$ is obtained from

$$F(\mathbf{x}_O) = \int_{\partial\Omega} L(\mathbf{x}_O, \mathbf{s}_O)\mathbf{s}_O \cdot \mathbf{n}_{\mathbf{x}_O} d\Omega(\mathbf{s}_O). \quad (1)$$

For the direct component, Beer–Lambert's law is integrated on the refraction-bent trajectories of all possible lines of sight connecting the lunar observer's site with the solar disk. At the solar disk, the Sun's emission radiance is scaled according to a specified limb-darkening function. For the scattered component, the solar photon trajectories are simulated by a Monte Carlo algorithm. The formulation is general enough to investigate both the umbra and penumbra phases of a lunar eclipse and, as discussed below, to predict the in-transit signature of extrasolar planets.

Figure 1 sketches how the refraction-bent rays are traced sunward from the observer's site and, in turn, how Equation (1) is evaluated for the direct sunlight component. In our numerical implementation of the integral, one ray is traced for each specified discrete element of $\mathbf{s}_O \cdot \mathbf{n}_{\mathbf{x}_O} d\Omega(\mathbf{s}_O)$. (Throughout this paper we refer to rays, although it would be more appropriate to refer to ray bundles.) Since the integration is carried out at $\mathbf{x}_O$, we do not have to correct for the optical phenomenon of attenuation by refraction (Link 1969). Attenuation by refraction is simply the reduction in the cross section (and therefore in the associated irradiance) of a ray bundle departing from the solar disk and reaching the observer's site after crossing Earth's atmosphere. In other formulations that use the solar plane for integrating Equation (1), this phenomenon must be explicitly introduced as a factor weighing the size of the emitting solar disk parcel and its refracted image at the planet's terminator (Link 1969). This effect would be especially important for rays crossing the lower layers of the atmosphere. Those are also the rays more strongly affected by gas and aerosol extinction.

The formulation holds valid for any combination of e and d_O, where e is the geocentric angular distance from the area of lunar disk being probed to the geometrical umbra center and d_O is the distance from the observer's site on the Moon to Earth's center. In the $d_O \to \infty$ limit, the formulation becomes relevant to the investigation of transiting extrasolar planets and e becomes a measure of the orbital phase. Numerically, we set $d_O \to \infty$ by assuming a sufficiently large d_O. Special care is taken to ensure that all the formulae occurring in the numerical implementation adopt the correct forms in that limit case.

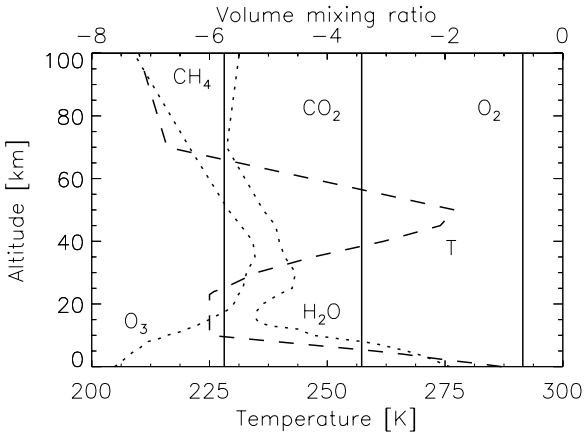

Figure 2. Vertical profiles of temperature (dashed curve) and volume mixing ratios (solid and dotted curves) in the nominal atmosphere.

3. THE ECLIPSE IN PROGRESS

We start by investigating the near-infrared spectra obtained at the WHT, looking for changes in their structure during the umbra phase of the eclipse. The exercise is useful to further validate our model of lunar eclipses and to show how the depth of molecular bands in the spectra varies as the eclipse progresses.

The nominal atmosphere in the simulations takes the temperature, O_3 and H_2O (vapor) profiles from the FSCATM subarctic summer model atmosphere (Gallery et al. 1983), and constant volume mixing ratios of 0.2094, 3.833×10^{-4}, and 1.779×10^{-6} for O_2, CO_2, and CH_4 (Hansen & Sato 2004), respectively. The vertical profiles of temperature and the volume mixing ratios are graphed in Figure 2. The density at all altitudes was determined by integration of the hydrostatic balance equation. For the collision-induced absorption (CIA) bands of oxygen at 1.06 and 1.27 μm, we proceeded as follows. For the $O_2\cdot O_2$ CIA band at 1.06 μm, we adopted the binary cross sections measured at 230 K in a 75%/25% mixture of O_2/N_2 by Smith & Newnham (2000). For the $O_2\cdot O_2$ + $O_2\cdot N_2$ CIA band at 1.27 μm, we used the binary cross sections measured at 253 K by Maté et al. (1999). Both sets were rescaled to have peak values in air of $1.7\times10^{-45}\times0.21 = 3.57\times10^{-46}$ and $1.7\times10^{-45}\times0.21\times4 = 1.43\times10^{-45}$ cm^5 molecule^{-2} at 1.06 and 1.27 μm, respectively. The selected band shapes and scaling factors are consistent with the conclusions drawn in a recent investigation of solar occultation data obtained with the SCIAMACHY spectrometer on board ENVISAT (García Muñoz & Bramstedt 2012). We evaluated the optical opacity for both CIA bands through $d\tau = \sigma_{\rm CIA}[O_2][X]ds$, where ds is the differential integration path, $[\cdot]$ stands for number density, X is the O_2 collision partner in the CIA band (O_2 at 1.06 μm and O_2 + N_2 at 1.27 μm), and $\sigma_{\rm CIA}$ are the binary cross sections. We set an opaque cloud layer with cloud tops at 6 km and an aerosol extinction profile at 1.02 μm about four times the 2008 September profile of Sioris et al. (2010). Further, we assumed that the aerosol optical properties are wavelength independent over the explored range of wavelengths. The nominal atmosphere is consistent with the findings by García Muñoz et al. (2011) from optical data of the same eclipse that point to a heavy aerosol loading following the eruption of the Kasatochi volcano one week ahead of the eclipse. Scattered sunlight is negligible longward of 1 μm and therefore omitted. The simulated spectra were convolved with a Gaussian line shape at a resolving power of about 1000.

A critical aspect in the comparison between observations and simulations is the solar elevation angle, e, or distance from the geometrical umbra center to the projection of the instrument's collecting element on the lunar disk. No images were taken of the slit projected on the Moon and e had to be estimated indirectly. For that purpose, we followed two different methods. Method (1) estimates e from the telescope pointing coordinates recorded in the FITS raw datafiles. The Sun, Earth, and Moon coordinates, the coordinates at the ORM, and the angular size of the lunar disk were taken from the JPL HORIZONS service (Giorgini et al. 1996). In method (2), we produced geocentric images of the lunar disk with the GeoViz software.[5] From the Moon's center, we displaced the slit south in equatorial declination on the image until only half of the 4.2 arcmin slit rested on the lunar disk. From the image, we recorded the coordinates of the mid-point projection of the slit on the lunar disk. Then, e was calculated as the geocentric angle from that point to the umbra center.

Figure 3 shows the set of 11 umbra spectra together with our model simulations. We arranged the zj and hk spectra in pairs according to the times of observation. Each pair contains data collected within an interval of no more than six minutes. To first approximation, each pair can be seen as an uninterrupted spectrum from 0.9 to 2.4 μm. For the model simulations, we adjusted the e parameter to ensure an optimal match of the eclipse data. In some cases, we modified the H_2O content by an amount that was always less than 10% of the nominal profile. The text in the graphs gives the time at mid-exposure and airmass for the Moon-to-telescope optical path, along with the estimated (e_1 and e_2) and adjusted ($e_{\rm adj}$) solar elevation angles. The quality of each match was judged by giving special weight to the O_2 and CIA bands in zj, and the CO_2 and CH_4 bands in hk. Absorption in both CIA bands remains linear throughout the eclipse. Indeed, we note the suitability of the CIA band at 1.06 μm, which occurs over a region only moderately affected by other molecular bands, for monitoring the Moon's progress across the umbra. Overall, the agreement between the eclipse data and the simulations is consistently good over the entire spectral range. Exceptions are the regions of strong water absorption at 1.35–1.45 and 1.8–2.1 μm, where the telluric correction introduces obvious artifacts. A more flexible implementation of aerosol extinction in the simulations would have surely improved the match between the observational and synthetic spectra, but it was judged that such an effort was not critical for the present purpose.

The minimum $e_{\rm adj}$ occurs at 21:12–21:16 UT, in fair agreement with the prediction of geometrical greatest eclipse for 21:10:06 UT.[6] The comparison between the estimated and adjusted angles indicates that e_1 and e_2 are systematically larger than $e_{\rm adj}$. The differences are typically $\sim0\overset{\circ}{.}05$ except in the 20:54–20:59 UT spectrum, in which case it reaches $\sim0\overset{\circ}{.}1$. This spectrum was acquired at a rather high airmass, and refraction in the Moon-to-telescope optical path may thus play a role. The 4.2 arcmin slit spans $\sim1/15$th of the lunar disk diameter. The sunlight that enters the slit arrives from a range of distances to the umbra center that may lead to differences in e of $\sim0\overset{\circ}{.}04$. Further, the non-uniform albedo of the Moon along the slit may move the effective slit center away from its geometrical location. It is thus difficult to define an equivalent solar elevation angle from purely geometrical considerations.

[5] New Horizons Geoviz by H. Throop, http://soc.boulder.swri.edu/nhgv/.
[6] Eclipse Predictions by F. Espenak, http://eclipse.gsfc.nasa.gov/eclipse.html.

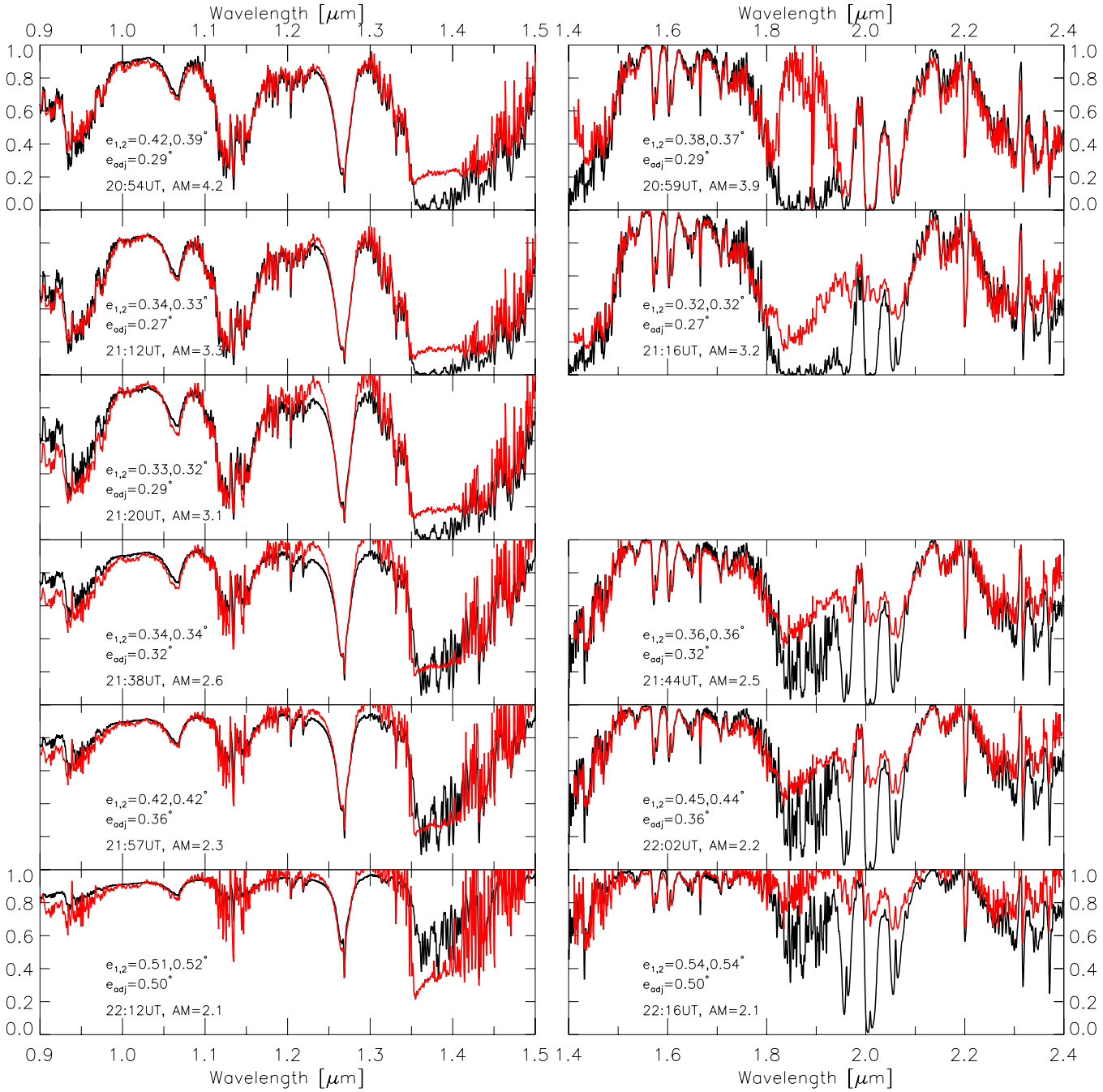

Figure 3. In red, the eclipse spectra in *zj* (left) and *hk* (right). In black, the model simulations. The text inset shows the estimated *e* angles and the *e* angle adjusted in the model simulation to match optimally the observed spectra. AM is the airmass for the Moon-to-telescope optical path.

(A color version of this figure is available in the online journal.)

In addition to the above arguments, one may also expect that local features in the atmosphere intercepted by the refracted sunlight rays will have an impact on $e_{\rm adj}$. To explore this possibility, we conducted a few simulations in modified conditions of clouds and aerosols. As a rule, setting the cloud tops below the nominal 6 km level leads to deeper absorption bands than in nominal conditions. If, for instance, the cloud tops are set at 3 km, the 21:12–21:16 UT eclipse spectra are optimally reproduced with $e \sim 0\overset{\circ}{.}29$, rather than $0\overset{\circ}{.}27$. The effect of low clouds on $e_{\rm adj}$ diminishes progressively as e increases. The nominal aerosol profile extends well up to ∼16–17 km and results in sunlight extinction over a broad range of altitudes. We verified that reducing the aerosol extinction to the 2008 September levels of Sioris et al. (2010) has a minor impact on the spectrum's structure near greatest eclipse.

Figure 4 (top) shows the 21:12–21:16 UT eclipse spectrum and the corresponding simulation. In Figure 4 (middle), the color lines are the contributions from H_2O, O_2, CO_2, CH_4, and the CIA bands of oxygen to the simulation. For $e \sim 0\overset{\circ}{.}3$, the sunlight rays that reach the area of lunar disk being probed have their closest approach to Earth's surface at altitudes in the range ∼2–11 km (García Muñoz & Pallé 2011). The range is effectively narrower because the lower altitudes are optically thick and, in addition, we assumed opaque clouds below 6 km. The spectrum of Figure 4 (top) is indeed well approximated by a limb-viewing transmission spectrum of the atmosphere as seen

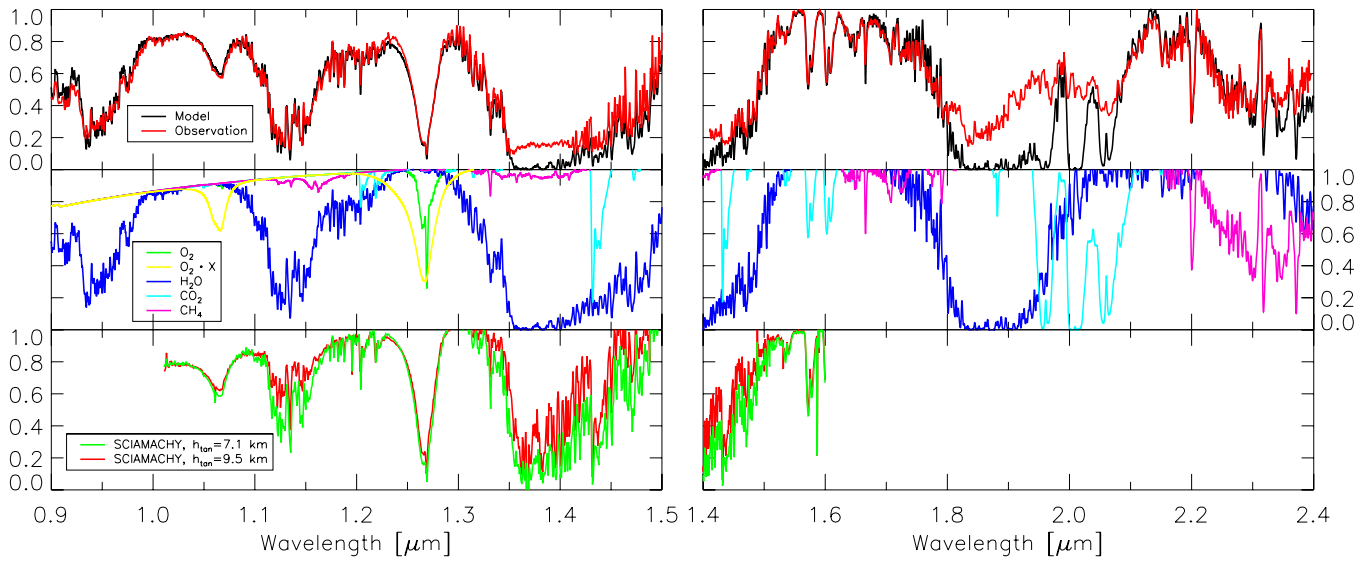

Figure 4. Top: lunar eclipse spectrum at 21:12–21:16 UT and model simulation. Middle: O_2, $O_2 \cdot X$, H_2O, CO_2, and CH_4 contributions to the model simulation. Bottom: SCIAMACHY solar occultation spectra measured from tangent altitudes of 7.1 and 9.5 km.

(A color version of this figure is available in the online journal.)

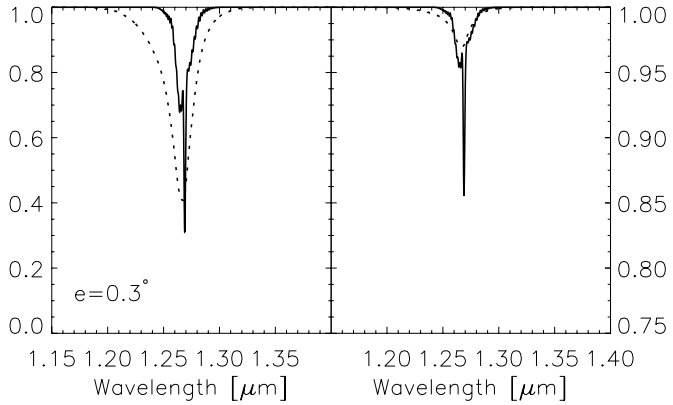

Figure 5. O_2 (solid) and CIA (dotted) absorption bands at 1.27 μm for e angles of 0.3 and 0.7. Far from the umbra center, the CIA band loses relative importance with respect to the monomer band.

from a tangent altitude of ∼10 km. For comparison, Figure 4 (bottom) shows two solar occultation spectra measured with the SCIAMACHY spectrometer for tangent altitudes of ∼7.1 and 9.5 km. The resemblance of the lunar eclipse spectrum to the SCIAMACHY spectra is apparent.

For $e \sim 0.5$ (still in the umbra), the range of altitudes of closest approach is ∼4–16 km, and for $e \sim 0.7$ (at the umbra/penumbra edge) it is ∼8–65 km. The shift and widening of the range of altitudes for closest approach has notable consequences on the spectrum's structure. For molecules whose densities decay monotonically with altitude, increasing e means the dilution in the spectrum of the molecular signature. This is due, first, to a diminished contribution from the atmosphere's optically thicker layers and, second, to a larger amount of light passing unattenuated through the upper altitudes. This effect is especially apparent for H_2O and the $O_2 \cdot O_2 + O_2 \cdot N_2$ collision complex because their densities drop at a faster rate than those of (nearly) well-mixed molecules such as O_2, CO_2, and CH_4. The simulations of the monomer and CIA bands of oxygen at 1.27 μm in Figure 5 illustrate this trend. For $e = 0.3$, the O_2:CIA equivalent widths are in a ratio of 1:3.3, whereas for $e = 0.7$, the ratio is only 1:0.9. Thus, as the observer probes regions of the lunar disk closer to the penumbra, the relative contributions of H_2O and the collision complex with respect to the other molecules tend to decrease.

3.1. The Impact of the Upper Atmosphere on Umbra Spectra

The umbra spectrum published by Pallé et al. (2009) with data of the 2008 August 16 event is representative of conditions near greatest eclipse (García Muñoz et al. 2011) and the atmosphere at mid-to-north latitudes over the Atlantic. At the relevant $e \sim 0.3$, the absorption features are formed in refracted sunlight ray trajectories that approach Earth's surface at minimum distances $\lesssim$11 km. The occurrence of strong H_2O and CIA band features confirms the importance of the lower altitudes.

Pallé et al. (2009) mention the identification of the Na I neutral atom at optical wavelengths in their published spectrum. The eclipse was contemporary with the meteor shower of the Perseids, which means that abnormally elevated amounts of that metal in the mesosphere and lower thermosphere might be expected (Plane 2003). Following Fussen et al. (2004), we estimate that in globally averaged conditions the optical thickness at the resolution of the umbra spectrum for the Na I doublet at 0.589 μm from a tangent altitude of 11 km is $\sim 2 \times 10^{-3}$. The sodium peak density is known to increase sporadically by factors of up to 10 in layers a few kilometer thick (which entails an increase in the integrated column by a factor of a few), sometimes over horizontal spans of hundreds of kilometers, especially during meteor showers (Moussaoui et al. 2010; Plane 2003; Dou et al. 2009). Even then, such a weak signature makes the detection of the Na I neutral atom challenging for a spectrum of moderate spectral resolution. Thus, our analysis indicates that the identification of the Na I doublet in the Pallé et al. (2009) spectrum is questionable and requires additional confirmation.

4. THE EARTH IN TRANSIT

4.1. The Earth–Sun System at Mid-transit

Everyday, sunsets offer real-life demonstrations of the refraction of sunlight in the atmosphere. Looking from the ground

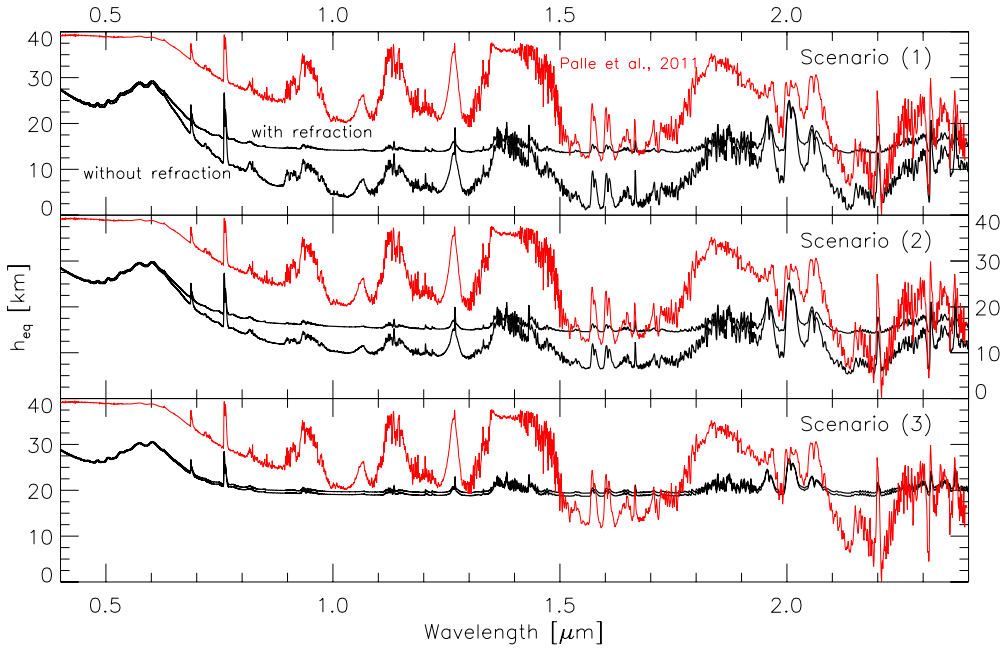

Figure 6. Equivalent heights for a refractive and a non-refractive atmosphere. Top panel: Rayleigh atmosphere. Middle panel: globally averaged conditions of clouds and aerosols. Bottom panel: aerosol-rich, cloudy atmosphere as described in Section 3. The red curve on each panel is the equivalent height as defined through the noise-free version of Equation (4) in Pallé et al. (2011): $h_{\rm eq} = h_{\rm TOA} \times (1 - \mathbb{T}_p)$ with $h_{\rm TOA} = 40$ km and where $\mathbb{T}_p$ is the umbra spectrum published by Pallé et al. (2009) normalized at its maximum near 2.2 μm.

(A color version of this figure is available in the online journal.)

over the horizon, the setting Sun appears about one solar diameter above its true elevation. Sunlight rays crossing the atmosphere and having their closest approach to Earth's surface at a tangent altitude $h_{\rm tan}$ are approximately refracted by an angle $\alpha_{\rm refr} \sim (n(h_{\rm tan}) - 1) \times (2\pi R_p/H)^{1/2}$ (Baum & Code 1953; Seager & Sasselov 2000). For a terrestrial radius $R_p \sim 6377$ km, a constant scale height $H \sim 8$ km and a typical refractivity at sea level in the optical $n(h_{\rm tan} = 0) - 1 \sim 2.8 \times 10^{-4}$, the end-to-end refracted angle estimated from the above equation is $\alpha_{\rm refr} \sim 1.^\circ 14$. Thus, over a distance of 1 AU, a ray incident on the planet that grazes Earth's surface is deflected by ~4.26 solar radii. Tracing the ray trajectories from a remote observer's site back toward the solar disk, one concludes that the mid-transit solar image at the observer's site is formed by sunlight rays having their closest approach to the planet's surface at densities ~1/4.26 or less than at the sea level. Further, our estimate suggests that, at mid-transit, refraction prevents the remote observer's access to altitudes within a $z_{\rm refr}$-sized ring above the planet's surface. The exact size of this refraction–exclusion ring can only be determined by integrating the ray trajectories through the atmosphere after prescribing the altitude-dependent refractivity of the atmospheric gas. Assuming, for the purpose of obtaining a first estimate, that the atmosphere is isothermal and that the refractivity decays with altitude as $\exp(-z/H)$, one obtains that $z_{\rm refr} \sim H \ln 4.26 \sim 11.6$ km. This approximate result is reached by equating the deflected distance of rays tangent at an altitude $z_{\rm refr}$ and the solar radius, i.e., $R_\odot = (n(h_{\rm tan} = 0) - 1)\exp(-z_{\rm refr}/H)(2\pi R_p/H)^{1/2} a_\odot$. Here, $R_\odot$ and $a_\odot$ stand for solar radius and the planet's orbital distance, respectively.

Our model simulations with the formulation of Section 2 in the $d_{\rm O} \to \infty$ limit provide refined magnitudes of the above estimates for $z_{\rm refr}$. For the nominal atmosphere described above, a sunlight ray grazing Earth's surface is refracted by ~1.°08 and only altitudes above $z_{\rm refr} \sim 13.2$ km contribute to the mid-transit signal measured at the observer's site. Thus, the mid-transit spectrum measured by the remote observer will lack the signature of the atmospheric layers containing the bulk of the spectroscopically active gases. The value of $z_{\rm refr}$ depends on the fluctuations in the atmosphere's density profile and water content through the refractivity of the gas. A sensitivity analysis perturbing those two parameters within the values in the model atmospheres of Gallery et al. (1983) shows that $z_{\rm refr}$ typically lies between 12 and 14 km.

Figure 6 displays in black the mid-transit spectrum of the Earth in two levels of approximation, namely with and without refraction, and three atmospheric scenarios. The scenarios represent (1) a Rayleigh atmosphere, free of clouds and aerosols; (2) an atmosphere with cloud tops at 2 km, the background aerosol extinction profile for 2007 September at about 1 μm published by Sioris et al. (2010) multiplied by $(1.02/\lambda\ [\mu{\rm m}])^{1.2}$ at other wavelengths; and (3) the aerosol-rich, cloudy atmosphere described in Section 3. The aerosol loading in scenario (2) might be seen as a plausible representation of globally averaged conditions (Hayashida & Horikawa 2001). The aerosol loading in scenario (3) is abnormally elevated for typical Earth conditions but may be representative of the atmosphere after a major volcanic eruption (García Muñoz et al. 2011). We note, however, that in our own solar system, Mars undergoes episodic events of abnormally elevated aerosol amounts being transported across the globe and thus affecting the aerosol loading on global scales, and that Venus is enshrouded by a complex system of clouds and haze layers up to pressures well below 1 atm.

We use the equivalent height, $h_{\rm eq}$, defined according to

$$\frac{F_p}{F_\odot} = 1 - \left(\frac{R_p + h_{\rm eq}}{R_\odot}\right)^2, \qquad (2)$$

to provide a measure of the atmosphere's thickness opaque to the incident sunlight. As a consistency check, the refractionless

calculations were tested against the more usual formulation for the in-transit stellar dimming (Hubbard et al. 2001):

$$\frac{F_p}{F_\odot} = \frac{2\pi \int_{R_p}^{R_\odot} \exp\left(-\tau(r_b)\right) r_b dr_b}{\pi R_\odot^2} \quad (3)$$

with:

$$\tau(r_b) = \int_{r_b}^{R_\odot} \frac{2 r_b \gamma(r) r / r_b}{\sqrt{(r/r_b)^2 - 1}} d(r/r_b), \quad (4)$$

where $\tau(r_b)$ is the optical thickness at an impact altitude $r_b - R_p$ and $\gamma(r)$ is the optical extinction coefficient at altitude $r - R_p$ above the planet's surface. The agreement between the two implementations proved to be excellent. It must be mentioned that Equation (4) was integrated in t, $= \cosh^{-1}(r/r_b)$, rather than in r/r_b, to avoid the singularity in the denominator of the integrand.

Figure 6 clearly shows how refraction removes much of the mid-transit spectrum's structure. An exception to that is the Chappuis band of ozone, which absorbs noticeably in all cases shortward of $\sim$0.8 μm. Terrestrial ozone densities peak in the stratosphere, and ozone in the refraction–exclusion ring contributes in a minor way to the disk-integrated signature. The features longward of 1 μm are readily identifiable by comparison with Figure 4. Shortward of 1 μm, the sharp features at 0.76, 0.69, and 0.63 μm are the $X(v'' = 0) \rightarrow b(v' = 0, 1, 2)$ bands of O_2, respectively. The remaining structure in that region is largely due to H_2O. With respect to the nearby continuum, the equivalent heights of the discrete features in the spectra of the refractive atmosphere are always less than $\sim$10 km in the 0.4–2.5 μm spectral range. In going from atmospheric scenarios (1) to (3) it is seen that refraction becomes less important as aerosol extinction near the $z_{\rm refr}$ boundary becomes dominant. The visual inspection of the transmission spectra published by Ehrenreich et al. (2006) and Kaltenegger & Traub (2009) for an Earth twin shows that their spectra are generally consistent with our refractionless calculations.

Were the Sun and Earth observed at mid-transit from a remote distance, the transmitted sunlight reaching the remote observer's site would be determined by sunlight photons crossing Earth's atmosphere at altitudes above $\sim$12–14 km. As seen in Figure 6, ignoring the refractive nature of Earth's atmosphere would mean a significant overestimation of most spectral features. The overestimation is more obvious when the model atmosphere is assumed free of clouds and aerosols since airborne particles act as natural barriers to the transmission of light through the lower altitudes. Because meteorological activity is largely confined to the troposphere, the planet's meteorology will have limited impact on the in-transit transmission spectrum.

The sunlight rays passing closer to the planet's surface at mid-transit originate from the near-limb region of the opposite solar hemisphere. In order to assess the impact of solar limb darkening, we repeated the calculation for the three scenarios described above, including a linear limb-darkening law for the solar brightness, $U = 1 - u_1(1 - \mu_\odot)$, and $u_1 = 0.6$ (Giménez 2006). To proceed with the comparison, we redefined $h_{\rm eq}$ in the way:

$$\frac{F_p}{F_\odot} = 1 - \frac{3}{3 - u_1} \left(\frac{R_p + h_{\rm eq}}{R_\odot} \right)^2,$$

to account for the $(3 - u_1)/3$ factor in the limb-darkened solar irradiance, $F_\odot$. Our model simulations indicate that $h_{\rm eq}$ differs by less than $\sim$1 km in the cases with $u_1 = 0$ and 0.6. Thus, solar limb-darkening affects in a negligible way the spectrum's structure at mid-transit.

As in Section 3, we calculated the equivalent widths of the monomer and CIA bands of oxygen at 1.27 μm. For the refractive calculations of scenarios (1)–(3), we obtained that the O_2:CIA equivalent widths are in ratios of 1:0.70, 1:0.64, and 1:0.47, respectively. The ratios indicate that the distinct identification of the CIA band becomes more and more difficult as the atmospheric opacity of aerosols and clouds increases.

García Muñoz & Pallé (2011) estimated that the sunlight scattered at Earth's terminator toward the eclipsed Moon could amount to up to $\sim 10^{-7}$ to 10^{-6} of the solar irradiance depending on the forward-scattering efficiency of the airborne aerosols. During the eclipse, the magnitude of scattered sunlight depends on the ratio of the solid angles subtended by the Earth, $\sim 1/d_{\rm O}^2$, and the Sun, $\sim 1/(d_{\rm O} + a_\odot)^2$, from the lunar observer's site on the Moon. In the lunar eclipse, we used for $d_{\rm O}$ and $a_\odot$, 382665.9 km and 1 Astronomical Unit, respectively. Thus, the amount of stellar light scattered toward the remote observer during the transit is $\sim (10^{-7}$–$10^{-6}) \times (d_{\rm O} + a_\odot)^2 / d_{\rm O}^2 \sim 10^{-12}$–$10^{-11}$, which is much less than the $\sim 10^{-4}$ dimming caused by the planet's core or the 10^{-7} to 10^{-6} dimming attributable to the strongest atmospheric features.

Next, we address under what conditions a lunar eclipse spectrum may be representative of the in-transit transmission spectrum of the remotely observed Earth–Sun system. Since at mid-transit only altitudes above $\sim$12–14 km are probed, the eclipse phases matching more closely that condition entail solar elevation angles $e \gtrsim 0.^\circ 9$, which are well within the penumbra (García Muñoz & Pallé 2011). Thus, spectra from the penumbra, rather than from the umbra, will be better representatives of the in-transit transmission spectrum for the Earth–Sun system. Figure 3 in García Muñoz & Pallé (2011) shows an eclipse spectrum at different phases. The comparison of that figure and our Figure 6 confirms that the eclipse spectrum tends to resemble the mid-transit transmission spectrum as the eclipse approaches the umbra/penumbra edge.

4.2. The Earth–Sun System Near Ingress/Egress

We have so far focused on the spectrum at mid-transit, noting the effect of refraction on the equivalent height of Earth's atmosphere with respect to the situation for a virtual non-refractive atmosphere. The refraction bending of sunlight rays does, however, introduce phase-dependent effects on the intensity and spectral structure of the transmitted sunlight that are worth exploring.

Out of transit, refraction causes the brightening of the planet's hemisphere more distant from the solar disk. This effect has been reported for Venus transits and causes a transient halo at the planet's limb that is readily discernible from Earth with the aid of a small telescope between internal and external contacts. It is attributed to Lomonosov back in the 18th century the correct interpretation of this halo, a fact that, in turn, meant the first evidence for an atmosphere at the planet (Link 1959). The last Venus transit occurred in 2004 June and provided numerous images of the halo that confirmed the pole-to-equator asymmetry in the optical properties of the planet's atmosphere (Pasachoff et al. 2011; Tanga et al. 2012). The contribution of the halo to the net brightness of the planet–star system is tiny for Venus but might amount to a detectable magnitude for transiting Jovian extrasolar planets on long-duration orbits (Sidis & Sari 2010).

The halo is a visual representation of the enhancement in the amount of refracted sunlight at the planet's outer hemisphere.

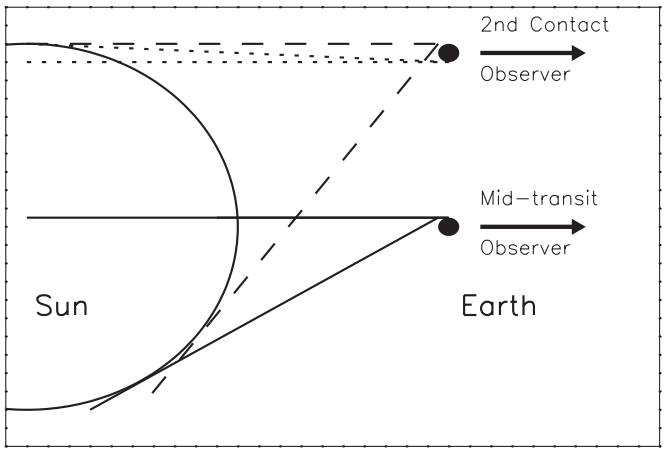

Figure 7. Earth–Sun system at mid-transit and at second contact. In each case, the sunlight that traverses Earth's limb originates from a different zone of the solar disk. At second contact, the outer hemisphere sees the entire solar disk, whereas the inner hemisphere sees only a narrow zone close to the Sun's edge.

This enhancement occurs together with a diminishment on the opposite hemisphere. Figure 7 sketches the situation. Sunlight rays passing through the outer hemisphere may be refracted by an angle of up to $\sim 2R_\odot/a_\odot$, whereas on the inner hemisphere refraction angles of more than $\sim 2R_p/a_\odot$ do not contribute to the signal collected by the distant observer. Different refraction angles also mean different depths of the sunlight rays into the atmosphere and, in turn, a refraction ring whose size is larger on the inner hemisphere than on the outer one.

The upper curves in Figure 8 represent the equivalent heights of the atmosphere from mid-transit ($e = 0°$) to internal contact ($e \approx 0.^\circ 2641$). We omitted limb darkening to emphasize the purely refractive effects, an assumption that enables us to use Equation (2) as a valid definition for the effective size of the atmosphere. The calculations assumed the Rayleigh atmosphere described above. The main conclusion to draw from that set of curves is that Earth's optical size varies with the phase of the transit as a result of the refraction of sunlight at the planet's limb. The Earth appears larger near internal contact than at mid-transit because in the proximity of the solar limb the optical enlargement of the inner hemisphere dominates over the shrinking of the outer one. The overall change in $F_p/F_\odot$ from mid-transit to internal contact amounts to about 3×10^{-7} for a variation in the equivalent height of 12 km. The detection of such a dimming in the stellar light appears extremely challenging, especially after considering that most of the drop occurs near ingress/egress where limb-darkening effects on the planet–star light curve are more prominent. The upper set of curves in Figure 8 also reveals that all molecular band features tend to weaken for phases that move away from mid-transit.

The lower set of curves in Figure 8 represent a measure of the halo brightness from external contact ($e \approx 0.^\circ 2690$) to phases well out of the eclipse. We use an equivalent halo thickness defined through

$$\frac{F_p}{F_\odot} = 1 + \frac{2\pi R_p h_{\rm halo}}{\pi R_\odot^2} \quad (5)$$

that gives the thickness of a ring around the planet of the same brightness as the Sun for $\mu_\odot = 1$. The effective halo thickness is about 10 km at external contact and decays as the planet moves farther out of transit. The net brightening at external contact is about 3×10^{-7} and, again, probably too faint for detection with the currently existing technology.

4.3. An Earth in Transit in a Different Planetary System

We have seen that at mid-transit refraction imposes a ring around Earth's terminator that deflects some line of sights from courses reaching the solar disk or, equivalently, some sunlight rays incident on the planet from courses reaching the remote observer. The size of this refraction–exclusion ring depends on the refractive properties of the atmosphere but also on the stellar radius and the planet's orbital distance. In standard conditions of temperature and pressure, the N_2 and O_2 refractivities are about 1.6 times less than the CO_2 refractivity but about twice the H_2 refractivity. For a virtual Earth twin whose atmospheric properties remained unchanged when placed in a planetary system other than ours, the ring will shrink if the planet is closer than 1 AU to the star ($a_s < a_\odot$) or if the host star is larger than one solar radius ($R_s > R_\odot$). The inequality $\alpha_{\rm refr} a_s/R_s > 1$ for the ratio of the refraction-deflected distance, $\alpha_{\rm refr} a_s$ (with $\alpha_{\rm refr} \sim 1°$), and the stellar radius establishes the approximate geometrical condition for which a refraction–exclusion ring exists at sub-atmospheric pressures. Speculations on possible values for $\alpha_{\rm refr} a_s/R_s$ find their justification in the wide variety of known planetary systems and the even wider variety that is likely to be discovered. As a matter of fact, Figure 6 applies to a broader range of $a_s/a_\odot$ and $R_s/R_\odot$ parameters than first stated. The lower synthetic curve represents approximately the condition $a_s/a_\odot \times R_\odot/R_s < 1$ and small enough so that refraction has a minor impact on the in-transit transmission spectrum. In turn, the upper synthetic curve represents the condition $a_s/a_\odot \times R_\odot/R_s \sim 1$. Those two curves bracket all possible conditions for the intermediate values of $a_s/a_\odot \times R_\odot/R_s$.

Oxygen is a potential biomarker and therefore constitutes a particularly appealing target for future searches. From our Figure 6, it is seen that the O_2 $X(0) \rightarrow b(0)$ band at 0.76 μm may be the best candidate for an oxygen search, although the CIA bands at 1.06 and 1.27 μm (the latter blended with the simultaneous monomer band) are also good candidates when the lowermost layers of the in-transit extrasolar planet are probed.

Although refraction will generally pose an additional challenge to the characterization of Earth-sized planets, the added difficulty may be minor in some configurations of interest. That is indeed the case for an Earth twin orbiting within the habitable zone (HZ) of some M-type stars, a planet–star combination that yields relatively favorable areal ratios. The HZ is the distance around a star in which a planet's water might be expected to exist in liquid state. Taking for the HZ the reference orbital distance quoted by Kaltenegger & Traub (2009), $a_s/a_\odot = (T_s/T_\odot)^2 (R_s/R_\odot)$, where, following our earlier convention, subscripts $_s$ and $_\odot$ denote stellar and solar magnitudes, respectively, one arrives at the condition, independent of R_s, $(T_s/T_\odot)^2 < (R_\odot/a_\odot)/\alpha_{\rm refr}$ for the stellar effective temperature below which refraction effects are minor. If we adopt $\alpha_{\rm refr} = 1.^\circ 08$ at the 1 atm pressure level, the condition becomes $T_s/T_\odot \leqslant 0.5$. Thus, an Earth twin that orbited within the HZ of an M-type star of effective temperature about 2900 K would produce mid-transit spectra with a closer resemblance to the refractionless simulations in Figure 6 than to the refractive simulation of the Earth–Sun system. Obviously, other intermediate situations would be possible for T_s values in between 2900 and 5800 K.

Discussing detectability issues for specific telescope sizes in the way it is done by Ehrenreich et al. (2006) or Kaltenegger &

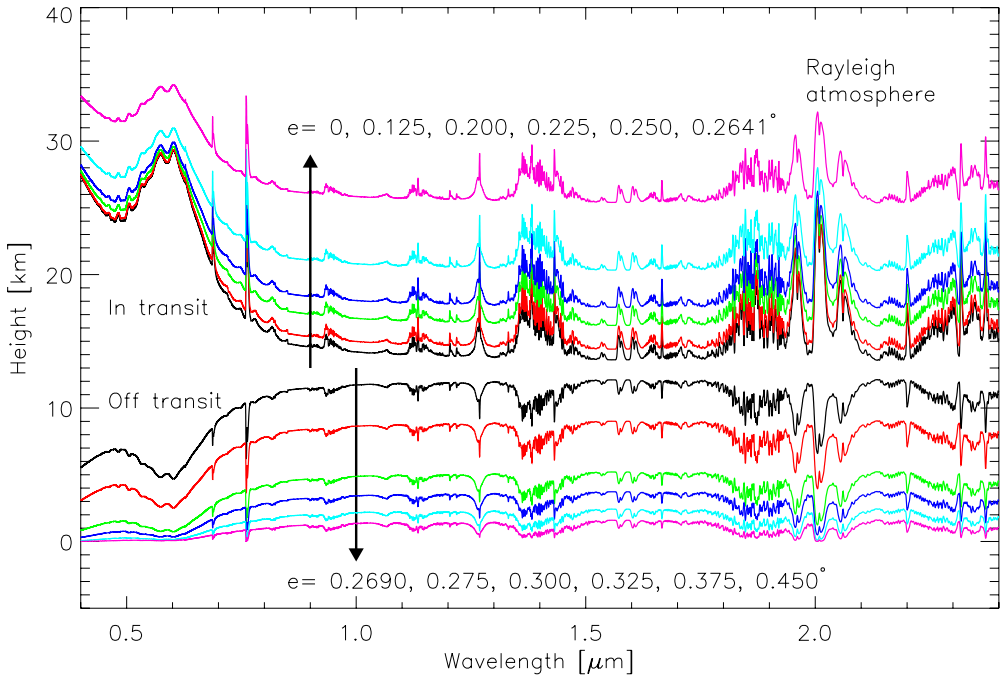

Figure 8. Equivalent heights for the Earth–Sun system in transit (upper set of curves) and halo heights for the system off transit (lower set of curves) at various phases (e). Limb darkening has been omitted to highlight the impact of refraction. For the in-transit curves, $h_{\rm eq}$ is defined through Equation (2), whereas for the off-transit curves, $h_{\rm eq}$ is defined through Equation (5). The calculations in this figure are specific to a Rayleigh atmosphere.

(A color version of this figure is available in the online journal.)

Traub (2009) is beyond the scope of our work. Kaltenegger & Traub (2009) do recognize the potential impact of refraction on the light curves of Earth-sized planets. They do not, however, give the size of the refraction ring in their investigation of the in-transit transmission spectrum of an Earth twin orbiting M-type stars nor explain the way refraction is implemented. The authors mention an altitude of 6 km below which the terrestrial atmosphere is opaque to grazing sunlight rays but do not state how much of that is contributed by refraction. As pointed out above, the size of the refraction–exclusion ring depends on the refractive properties of the atmosphere but also on both the stellar radius and the planet's orbital distance. Since Ehrenreich et al. (2006) account in some cases for the presence of clouds at altitudes of up to 10 km, the conclusions drawn from their cloudy models of an Earth twin might be appropriate for specific conditions in which refraction plays a significant role.

Pallé et al. (2011) discussed the in-transit detectability of the strongest absorption features from 0.4 to 2.4 μm using scaled versions of the Pallé et al. (2009) umbra spectrum. Setting the noise terms to zero in Equation (4) of Pallé et al. (2011), the equivalent height proposed in that work can be written as $h_{\rm eq} = h_{\rm TOA} \times (1 - \mathbb{T}_p)$, where $h_{\rm TOA}$ is a specified top-of-the-atmosphere height and $\mathbb{T}_p$ is the umbra spectrum normalized to one near 2.2 μm. Our Figure 6 shows in red the resulting equivalent heights for the specific case $h_{\rm TOA} = 40$ km investigated in Pallé et al. (2011). The comparison with the upper (black) synthetic curve in the top panel demonstrates that for an Earth-like extrasolar planet lacking aerosols and clouds and close enough to a solar-type star so that refraction effects are minor, the approach followed by Pallé et al. (2011) overestimates moderately the model predictions for a Rayleigh atmosphere. This is because the umbra spectrum published by Pallé et al. (2009) results from probing preferentially the lowermost altitudes of the atmosphere during the eclipse. In all other cases displayed in Figure 6, and more especially when refraction effects play a role, the equivalent heights for $h_{\rm TOA} = 40$ km in Pallé et al. (2011) are larger by up to an order of magnitude than the current model predictions. It is apparent that fainter features will impose tougher requirements on their detectability.

5. CONCLUDING REMARKS

We investigated lunar eclipses of the Earth and the transits of Earth-like extrasolar planets in a comparative manner. The Moon in umbra receives unscattered sunlight that has been transmitted through a section of the terrestrial atmosphere dictated by refraction. The diffuse sunlight that arrives at the eclipsed Moon is scattered from the entire terminator. During the transit of the Earth–Sun system, at mid-event, the refracted sunlight is transmitted through an annular ring that fully encloses the planet. The refraction bending of sunlight rays prevents sunlight rays passing through a refraction–exclusion ring above the planet's surface from reaching the remote observer. For the Earth–Sun system, at mid-transit, this ring extends up to 12–14 km, thus blocking the observer's access to the denser atmospheric layers. It may be stated that umbra eclipses maximize the contribution of the lowermost atmosphere and, to some extent, of scattered sunlight, whereas during the transit of an Earth-like extrasolar planet the transmitted signal is dominated by altitudes above a refraction–exclusion ring and scattered sunlight becomes negligible.

In the course of this work it has become apparent that a genuine transmission spectrum of the Earth in transit as observed from a remote distance is more difficult to obtain than what had been anticipated. Lunar eclipse spectra obtained during the penumbra are more representative of the in-transit spectrum than those obtained during the umbra. In the context of Earth-like extrasolar planets, the lunar eclipse spectra are helpful to fine tune synthetic spectra incorporating the fairly good knowledge

of the atmosphere obtained over decades of Earth's atmospheric research.

Refraction will affect the light curves of transiting Earth-like extrasolar planets. Its significance will depend on the refractive properties of the planet's atmosphere, the stellar size, and the planet's orbital distance. All these factors must be considered in the future to predict and/or interpret the light curves of such planets. The role of refraction will not be critical for Earth twins orbiting within the HZ of M-type stars with effective temperatures of about 2900 K and less. Finally, it is worth noting that recent lunar eclipse observations have contributed critically to bring up the importance of refraction in the future characterization of Earth-like extrasolar planets.

The near-infrared spectra discussed in Section 3 were obtained with the William Herschel Telescope at the Spanish Observatorio del Roque de los Muchachos of the Instituto de Astrofísica de Canarias. M.R.Z.O. and P.M.R. acknowledge support from projects AYA2010-21308-C03-02 and CGL2009-10641, respectively. E.L.M. is grateful for financial support from RoPACS, a Marie Curie Initial Training Network funded by the European Commission's Seventh Framework Program, and by the CONSOLIDER-INGENIO GTC project.

A.G.M. acknowledges G. T. Fraser for providing the Maté et al. (1999) binary cross sections and K. Bramstedt and the European Space Agency for the SCIAMACHY solar occultation spectra. Both M.R.Z.O. and E.L.M. acknowledge support from project AYA 2011-30147-C03-03.

REFERENCES

Batalha, N. M., Borucki, W. J., Bryson, S. T., et al. 2011, ApJ, 729, 27
Baum, W. A., & Code, A. D. 1953, AJ, 58, 108
Berta, Z. K., Charbonneau, D., Désert, J.-M., et al. 2012, ApJ, 747, 35
Brown, T. M. 2001, ApJ, 553, 1006
Charbonneau, D., Brown, R. M., Noyes, R. W., & Gilliland, R. L. 2002, ApJ, 568, 377
Charbonneau, D., Zachory, B. K., Irwin, J., et al. 2009, Nature, 462, 891
Désert, J., Lecavelier des Etangs, A., Hébrard, G., et al. 2009, ApJ, 699, 478
Dou, X.-K., Xue, X.-H., Chen, T.-D., et al. 2009, Ann. Geophys., 27, 2247
Ehrenreich, D., Tinetti, G., Lecavelier des Etangs, A., Vidal-Madjar, A., & Sensis, F. 2006, A&A, 448, 379
Fussen, D., Vanhellemont, F., Bingen, C., et al. 2004, Geophys. Res. Lett., 31, L24110
Gallery, W. O., Kneizys, F. X., & Clough, S. A. 1983, Environmental Research Paper ERP-828/AFGL-TR-83-0065, Hanscom
García Muñoz, A., & Bramstedt, K. 2012, J. Quantum. Spectrosc. Radiat. Transfer, 113, 1566
García Muñoz, A., & Pallé, E. 2011, J. Quantum. Spectrosc. Radiat. Transfer, 112, 1609
García Muñoz, A., Pallé, E., Zapatero Osorio, M. R., & Martín, E. L. 2011, Geophys. Res. Lett., 38, L14805
Giménez, A. 2006, A&A, 450, 1231
Giorgini, J. D., Yeomans, D. K., Chamberlin, A. B., et al. 1996, BAAS, 28, 1158
Hansen, J., & Sato, M. 2004, Proc. Natl Acad. Sci., 101, 16109
Hayashida, S., & Horikawa, M. 2001, Geophys. Res. Lett., 28, 4063
Hubbard, W. B., Fortney, J. J., Lunine, J. I., et al. 2001, ApJ, 560, 413
Hui, L., & Seager, S. 2002, ApJ, 572, 540
Kaltenegger, L., & Traub, W. A. 2009, ApJ, 698, 519
Léger, A., Rouan, D., Schneider, J., et al. 2009, A&A, 506, 287L
Link, F. 1959, Bull. Astron. Inst. Czech., 10, 105
Link, F. 1962, in Physics and Astronomy of the Moon, ed. Z. Kopal (New York: Academic), 161
Link, F. 1969, Eclipse Phenomena in Astronomy (Berlin: Springer), 205
Lissauer, J. J., Fabrycky, D. C., Ford, E. B., et al. 2011, Nature, 470, 53
Manchado, A., Fuentes, F. J., Prada, F., et al. 1998, Proc. SPIE, 3354, 448
Maté, B., Lugez, C., Fraser, G. T., & Lafferty, W. J. 1999, J. Geophys. Res., 104, 30585
Mayor, M., Bonfils, X., Forveille, T., et al. 2009, A&A, 507, 487
Moussaoui, N., Clemesha, B. R., Holzlöhner, R., et al. 2010, A&A, 511, A31
Pallé, E., Zapatero Osorio, M. R., Barrena, R., Montañés-Rodríguez, P., & Martín, E. L. 2009, Nature, 459, 814
Pallé, E., Zapatero Osorio, M. R., & García Muñoz, A. 2011, ApJ, 728, 19
Pasachoff, J. M., Schneider, G., & Widemann, T. 2011, ApJ, 141, 112
Plane, J. M. C. 2003, Chem. Rev., 103, 4963
Rauer, H., Gebauer, S., von Paris, P., et al. 2011, A&A, 529, A8
Seager, S., & Sasselov, D. D. 2000, ApJ, 537, 916
Sidis, O., & Sari, R. 2010, ApJ, 720, 904
Sing, D. K., Désert, J., Lecavelier Des Etangs, A., et al. 2009, A&A, 505, 891
Sioris, C. E., Boone, C. D., Bernath, P. F., et al. 2010, J. Geophys. Res., 115, D00L14
Smith, K. M., & Newnham, D. A. 2000, J. Geophys. Res., 105, 7383
Swain, M. R., Tinetti, G., Vasisht, G., et al. 2009, ApJ, 704, 1616
Tanga, P., Widemann, T., Sicardy, B., et al. 2012, Icarus, 218, 207
Tinetti, G., Vidal-Madjar, A., Liang, M.-C., et al. 2007, Nature, 448, 169
Ugolnikov, O. S., & Maslov, I. A. 2006, J. Quantum Spectrosc. Radiat. Transfer, 102, 499
Ugolnikov, O. S., & Maslov, I. A. 2008, J. Quantum Spectrosc. Radiat. Transfer, 109, 378
Vidal-Madjar, A., Arnold, L., Ehrenreich, D., et al. 2010, A&A, 523, A57
Vidal-Madjar, A., Désert, J.-M., Lecavelier des Etangs, A., et al. 2004, ApJ, 604, L69
Vidal-Madjar, A., Lecavelier des Etangs, A., Désert, J.-M., et al. 2003, Nature, 402, 143